

Tribological Investigation of K Type Worm Gear Drives

Balázs Magyar¹, Bernd Sauer¹, Péter Horák²

¹ TU Kaiserslautern, Institute of Machine Element, Gears and Transmissions
Gottlieb-Daimler Str. Geb. 42, D-67661 Kaiserslautern, Germany
magyar@mv.uni-kl.de; sauer@mv.uni-kl.de

² Budapest University of Technology and Economics, Department of Machine-
and Product Design, Müegyetem rkp. 3, H-1111 Budapest, Hungary
horak.peter@gt3.bme.hu

Abstract: This paper presents a calculation method to determine the locally changing tooth friction coefficient along each contact line based on the TEHD lubrication theory for worm gear drives operating in mixed lubrication conditions. This also involves a detailed presentation of a procedure to specify the proportions of boundary lubrication and hydrodynamic lubrication as well as temperature states in contact. By comparing the calculated tooth friction coefficients with experimental test results, it can be stated that the calculated results properly approximate the measurement results.

Keywords: worm gear drive; TEHD lubrication theory; mixed lubrication; numerical and experimental investigation; tooth friction coefficient

1 Introduction

There are different theories for the tribological investigation of gear teeth contact. Niemann [1] calculated the lubricant behaviour of worm gears according to the hydrodynamic lubrication theory. Wilkesmann [2] developed an algorithm to determine the speed and contact properties and losses of various worm gear drives of standard profiles. Predki [3] applied the elastohydrodynamic lubrication theory to evaluate the thickness of the lubricating film considering the deflection of the shaft. Bouché [4] considered the surface roughness and calculated the friction power loss of the worm gear teeth by assuming the mixed lubrication condition between the tooth surfaces. The aims of our investigation are to calculate the locally changing tooth friction coefficient of worm gear drives and to compare the calculated results with experimental tests. A knowledge of the tooth friction coefficient is necessary for further investigation into the dynamic behaviour of worm gear drives.

2 Geometry and Kinematics of the Investigated Drive

This study examines a worm gear set of $a=100$ mm axial distance, ZK profile, and $i=40$ ratio, with the worm shaft located at the bottom.

Knowledge of contact lines is required for determining the tribological properties of worm gear sets. Contact line points associated with the traverse positions of the worm shaft can be determined by a numerical solution of the equation of meshing. According to the equation of meshing, the normal vector (\underline{n}) of the common surface is perpendicular to the relative velocity vector (\underline{v}) of the bodies at the contact point [6]:

$$f(\theta, \zeta, \varphi_1) = \underline{n} \cdot \underline{v} = 0 \quad (1)$$

Figure 1 shows instantaneous contact lines in case of the teeth parameters specified above, in 3 views, with different φ_1 angular position of the worm, in a stationary system of coordinates fixed to the casing $[x_1, y_1, z_1]$.

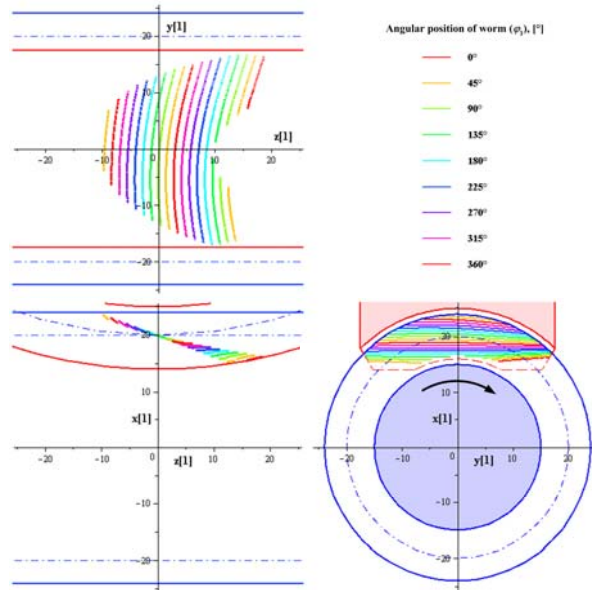


Figure 1
Contact lines calculated in a coordinate system fixed to the housing

Further tribological calculations require knowledge of speed and curvature properties at the contact line points. Speed conditions are determined in the manner described by Predki [3] and Bouché [4]. A kinematic procedure was developed by Litvin [6] to determine the contact point curvatures for spatial gears.

For the worm gear set examined, Figure 2 shows the course of v_{sliding} sliding velocity and the course of v_{Σ} effective sum velocity along the contact lines at an input rpm of $n_1=1500$ 1/min in the transverse section of the worm gear set.

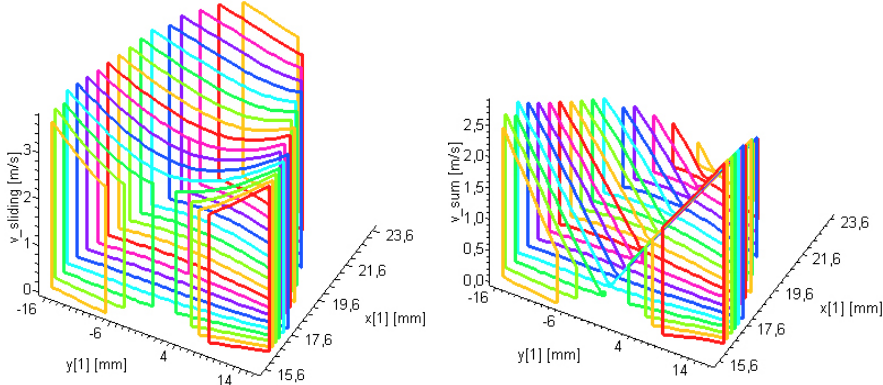


Figure 2

Changes in sliding velocity and in effective sum velocity along contact lines (transverse section)

As shown in Figure 2, sliding velocity does not change considerably along contact lines. On the contrary, there are significant changes in effective sum velocity. At entry (where the velocity of the worm shaft and the wheel are in the opposite direction) it assumes a large value. At the middle of the tooth, it is reduced to zero and it reaches its maximum at exit (here the velocity of the worm shaft and the wheel are in the same direction). Figure 3 shows the changes in ρ_E reduced radii of curvature.

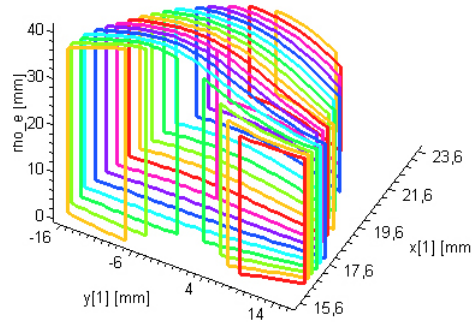


Figure 3

Changes in reduced radii of curvature along contact lines (transverse section)

3 Tribological Simulation

In the dimensions examined, the worm gear flanks operate in a mixed lubrication state [7]. This means that the asperities of contacting teeth are only partly separated by the film created. A precondition for determining the friction coefficient is to obtain the proportions of load distribution between the asperities and the film and the friction coefficient associated with boundary and hydrodynamic lubrication, respectively.

3.1 Model of the TEHD Lubrication of Worm Gear Teeth

In order to calculate these tribological properties, tooth flanks must be discretized. In the course of meshing, the worm shaft and the wheel are in contact with each other along the lines described above (see Figure 1). Between two contact points of a single contact line, tooth flanks can be substituted by rolls whose radius coincides with the reduced radius of curvature of tooth flanks, and the rolls perform rotational motion of the same or opposite direction at the velocity valid for the given contact point. This conceptual model is shown in Figure 4. This approximation, coming from Niemann [1], was successfully applied by Predki [3], as well as by Bouché [4].

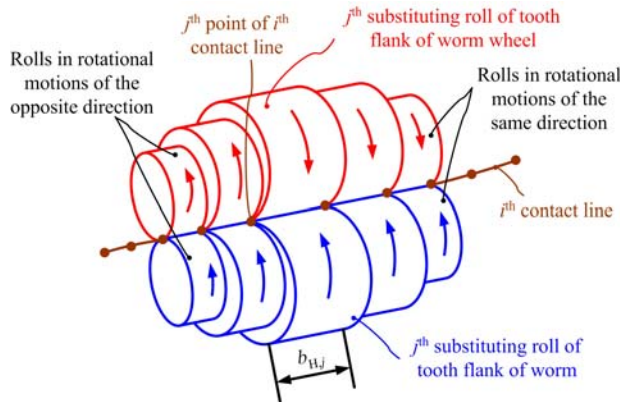


Figure 4
Substituting rolls for the tribological modelling of meshing

Based on the output torque, the height of the rolls, and the reduced radii of curvature, the load of each of the rolls and their deformations can be determined on the basis of Hertz's theory [4]. In the knowledge of these data, the EHD lubrication theory can be applied to substituting rolls for calculating the film thickness between tooth flanks. In our investigations, equal Stribeck's contact pressure is assumed to exist along the length of a roll. The pressure mound above

the flattening was approached according to Hertz, since the relatively low contact load-bearing capacity of the worm wheel made of bronze cannot produce pressures to give rise to a Petrushevich's peak and to narrow down the lubrication gap in the exit area. Accordingly, a lubrication gap of constant height was assumed for the entire contact area.

3.2 Determining Film Thickness between Substituting Rolls

Venner published a combined equation to determine minimum film thickness (h_{\min}) [8]. This equation yields accurate results in all four EHD ranges defined by Johnson [5]. The equation can be stated in the following form:

$$H_{\min} = \left[\left\{ (0,99 \cdot M^{-1/8} \cdot L^{3/4} \cdot t)^r + (2,05 \cdot M^{-1/5})^r \right\}^{s/r} + (2,45 \cdot M^{-1})^s \right]^{1/s}, \quad (2)$$

$$t = 1 - \exp \left\{ -3,5 \cdot M^{1/8} \cdot L^{-1/4} \right\},$$

$$r = \exp \left\{ 1 - 3 / (L + 4) \right\},$$

$$s = 3 - \exp \left\{ -1 / (2 \cdot M) \right\}$$

where H , L and M are dimensionless EHD parameters. This equation yields the minimum film thickness under isothermal conditions. Murch and Wilson introduced a thermal correction factor (ϕ_g) [9] for determining film thickness even in non-isothermal conditions. This correction factor depends on oil viscosity (η_0), the temperature dependence of oil viscosity (β), the thermal conductivity of oil (λ_g), and effective sum velocity (v_Σ).

$$\phi_g = \frac{3,94}{3,94 + \left(\frac{\eta_0 \cdot \beta \cdot v_\Sigma^2}{\lambda_g} \right)^{0,62}} \quad (3)$$

In order to determine the central non-isothermal lubrication gap size (h_0), the h_{\min} film thickness yielded by Venner's equation must be multiplied by 1.2 and the Murch and Wilson's correction factor [10]:

$$h_0 = 1,2 \cdot \phi_g \cdot h_{\min} \quad (4)$$

Figure 5 shows changes in the central non-isothermal film thickness thus determined for the worm gear drive examined, in the case of $n_1=1500$ 1/min input rpm, $T_2=570$ Nm output torque, and FVA 4 mineral oil lubrication, at $\vartheta_S=60^\circ\text{C}$ oil bath temperature. As can be seen, film thickness is affected by changes in effective sum velocity. Maximum film thickness is assumed at the end of contact lines; its value is reduced to zero at the middle.

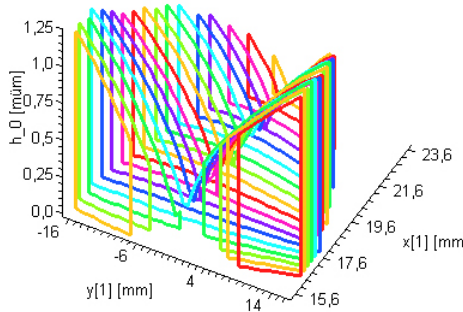


Figure 5

Changes in non-isothermal central film thickness along contact lines (transverse section)

3.3 Determining the Proportions of Friction Mechanisms

As a part of the present investigations, a calculation method was developed for determining the proportions of boundary lubrication and hydrodynamic lubrication. This requires knowledge of the roughness and material properties of contacting surfaces and of dimensionless film thickness.

The first model to describe rough surfaces – still frequently applied today – was developed by Greenwood and Williamson (the GW model) [11]. According to this model, asperities can be modelled by spherical caps of identical radius but stochastic height, and material properties are isotropic. Contact between two rough surfaces can be perceived as contact between a derived rough surface modelled by spherical caps and a smooth surface. The GW model also assumes that spherical caps do not affect adjacent spherical caps and that deformation is brought about only within single spherical caps (see Figure 6).

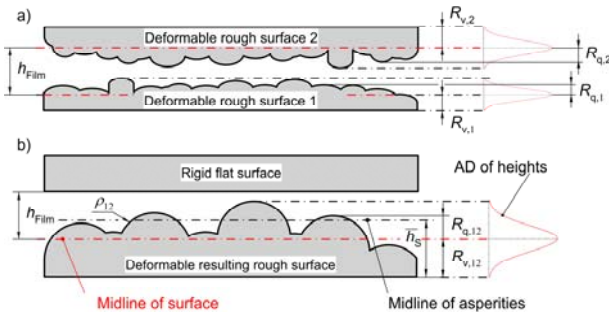


Figure 6

Generating derived surfaces from rough surfaces based on the GW model a) Two contacting rough surfaces, b) Contact model of a rigid flat surface and a deformable rough surface

The ρ_{12} radius of derived spherical caps can be specified by reduced radius generation according to the Hertzian theory:

$$\frac{1}{\rho_{12}} = \frac{1}{\rho_1} + \frac{1}{\rho_2} \quad (6)$$

The maximum valley depth ($R_{v,12}$) and rms-roughness ($R_{q,12}$) of the derivative surface can be calculated by the following correlations:

$$R_{v,12} = R_{v,1} + R_{v,2} \quad (7)$$

$$R_{q,12} = \sqrt{R_{q,1}^2 + R_{q,2}^2} \quad (8)$$

These values can be used for calculating the average height (h_s) and the standard deviation of heights (σ_s) of derivative spherical caps as follows:

$$\bar{h}_s = R_{v,12} + 0,82 \cdot R_{q,12} \quad (9)$$

$$\sigma_s = 0,71 \cdot R_{q,12} \quad (10)$$

Assuming that the height of asperities follows a Gaussian distribution, the probability density function of the derivative surface can be stated in the following form by using (9) and (10) [12]:

$$\varphi(h_s) = \frac{1}{\sqrt{2 \cdot \pi}} \cdot \exp \left(-\frac{1}{2} \cdot \left(\frac{h_s - \bar{h}_s}{\sigma_s} \right)^2 \right) \quad (11)$$

According to the GW model, contacts between each deformable spherical cap and the rigid flat surface can be examined separately. A spherical cap will first suffer elastic deformation then plastic deformation (see Figure 7).

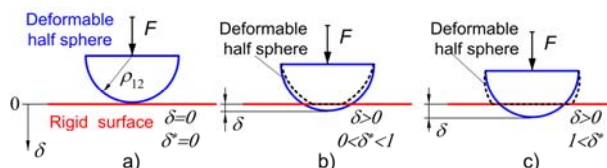


Figure 7
Contact model of a deformable half sphere and a rigid flat surface
a) contact, b) elastic deformation, c) plastic deformation

The boundary of elastic and plastic deformation is a distinctive point. The force to generate elastic deformation is called critical force (F_{Krit}), and the associated deformation is called critical deformation (δ_{krit}). Force and deformation figures are normalized by these values.

In the knowledge of spherical cap height, film thickness determines the rate of deformation δ of the spherical cap (see Figures 6 and 7).

The force F between the surfaces can be determined from this deformation δ . The present calculations used these complex equations to determine the force generated by deformation.

In order to determine the proportions of friction mechanisms, the generation of reduced surfaces is followed by film thickness modifications between a maximum value and zero, and the force arising between each contacting spherical cap and the rigid flat surface is determined for each film thickness, as well as its relation to the force that would arise in the case of nothing but boundary lubrication. This way a curve can be produced to represent the rate of boundary lubrication (ψ) in function of dimensionless film thickness (λ). Figure 8 shows curves determined by this procedure for steel-steel contact pairs of 3 different roughness levels.

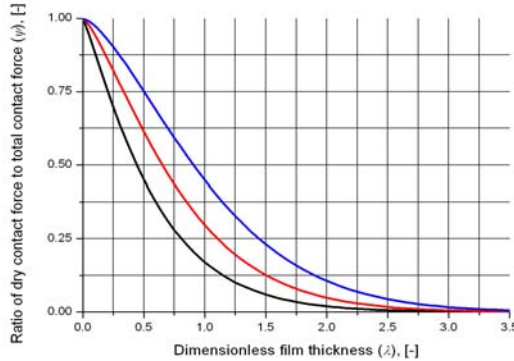


Figure 8

Separation curves of frictions mechanisms determined for steel-steel contact pairs of 3 different roughness levels

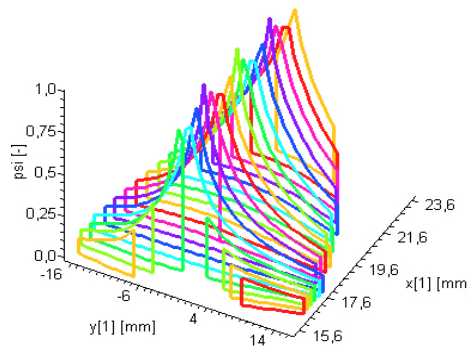


Figure 9

Changes in the proportion of boundary lubrication along contact lines (transverse section)

Figure 9 shows the proportions of boundary lubrication at the worm gear drive examined along contact lines, in case of $n_1=1500$ 1/min input rpm, $T_2=570$ Nm output torque and FVA 4 mineral oil lubrication, at $\vartheta_s=60^\circ\text{C}$ oil bath temperature.

At the middle of the tooth, where the film is reduced nearly to zero, is predominantly characterized by boundary lubrication.

3.4 Calculations of Temperature

It is essential to know the temperature course of the contact zone to be able to determine hydrodynamic lubrication.

It can be observed that the heat flow generated in the course of friction ($\dot{q}_{\text{friction}}$) exits to adjacent walls by conduction (\dot{q}_1, \dot{q}_2), and heats up the oil by convection (\dot{q}_k):

$$\dot{q}_{\text{friction}} = \dot{q}_1 + \dot{q}_2 + \dot{q}_k \quad (12)$$

The temperature course of both the oil film and the contacting surfaces is to be determined on this basis.

3.4.1 Surface Temperature Calculations

The point of departure for determining surface temperatures is Fourier's Law for heat conduction, to be stated generally in the following form:

$$c \cdot \rho \cdot \frac{\partial \vartheta}{\partial t} = -\text{div}(-\lambda \cdot \text{grad } \vartheta) \quad (13)$$

Assuming that heat conduction is effected only in the direction of motion (x direction) and into the specimens (y direction), and that material properties are constant, and by taking the motion velocity of the specimens (v_1, v_2) into consideration, equation (12) will be simplified to the following form (index 1 pertains to the worm shaft, and index 2 to the worm wheel):

$$\begin{aligned} \frac{c_1 \cdot \rho_1 \cdot v_1}{\lambda_1} \cdot \frac{\partial \vartheta_1}{\partial x} - \left(\frac{\partial^2 \vartheta_1}{\partial x^2} + \frac{\partial^2 \vartheta_1}{\partial y^2} \right) &= 0 \\ \frac{c_2 \cdot \rho_2 \cdot v_2}{\lambda_2} \cdot \frac{\partial \vartheta_2}{\partial x} - \left(\frac{\partial^2 \vartheta_2}{\partial x^2} + \frac{\partial^2 \vartheta_2}{\partial y^2} \right) &= 0 \end{aligned} \quad (14)$$

Gnilke developed a procedure to solve these equations, determining the course of temperature in the form of Fourier Integrals [13]. This procedure was further developed by Plote to determine the temperature distribution of bodies moving into both identical and opposite directions [14].

Based on [14], surface temperature rises can be stated in a dimensionless form as follows:

$$\theta_1 = \frac{\lambda_1 \cdot q_1}{\mu \cdot p_H \cdot v_S \cdot a_H}, \quad \theta_2 = \frac{\lambda_2 \cdot q_2}{\mu \cdot p_H \cdot v_S \cdot a_H} \quad (15)$$

On the basis thereof, the dimensionless form of Fourier's equation for heat conduction can be stated as follows:

$$\begin{aligned} Pe_1 \cdot \frac{\partial \theta_1}{\partial \bar{x}} - \left(\frac{\partial^2 \theta_1}{\partial \bar{x}^2} + \frac{\partial^2 \theta_1}{\partial \bar{y}^2} \right) &= 0 \\ Pe_2 \cdot \frac{\partial \theta_2}{\partial \bar{x}} - \left(\frac{\partial^2 \theta_2}{\partial \bar{x}^2} + \frac{\partial^2 \theta_2}{\partial \bar{y}^2} \right) &= 0 \end{aligned} \quad (16)$$

Where Pe_1 and Pe_2 are Peclét numbers to be specified as follows:

$$Pe_1 = \frac{c_1 \cdot \rho_1 \cdot v_1 \cdot a_H}{\lambda_1}, \quad Pe_2 = \frac{c_2 \cdot \rho_2 \cdot v_2 \cdot a_H}{\lambda_2} \quad (17)$$

Surface temperature rises can be determined in the following manner from differential equation (17), by disregarding the inferences included in [14], and using Fourier Integrals:

$$\begin{aligned} \theta_1(\bar{x}) &= \frac{1}{\pi} \int_0^\infty [c_{11} \cdot \cos(\bar{x} \cdot \varphi_z) - c_{12} \cdot \sin(\bar{x} \cdot \varphi_z)] \cdot d\varphi_z \\ \theta_2(\bar{x}) &= \frac{1}{\pi} \int_0^\infty [c_{21} \cdot \cos(\bar{x} \cdot \varphi_z) - c_{22} \cdot \sin(\bar{x} \cdot \varphi_z)] \cdot d\varphi_z \end{aligned} \quad (18)$$

The solution of (18) requires that the dimensionless flux of heat also be expressed by Fourier Integrals; this can be stated as follows:

$$\begin{aligned} \dot{Q}(\bar{x}, z) &= \frac{\dot{q}(\bar{x})}{\mu \cdot v_S \cdot p_H} = \frac{1}{\pi} \int_0^\infty [a_Q(\varphi_z) \cdot \cos(\bar{x} \cdot \varphi_z) + b_Q(\varphi_z) \cdot \sin(\bar{x} \cdot \varphi_z)] \cdot d\varphi_z, \\ a_Q(\varphi_z) &= \int_{\bar{x}_1}^{\bar{x}_2} [\dot{Q}(\bar{x}, z) \cdot \cos(\bar{x} \cdot \varphi_z)] \cdot d\bar{x}, \\ b_Q(\varphi_z) &= \int_{\bar{x}_1}^{\bar{x}_2} [\dot{Q}(\bar{x}, z) \cdot \sin(\bar{x} \cdot \varphi_z)] \cdot d\bar{x} \end{aligned} \quad (19)$$

Two more boundary conditions are required for determining c_{ij} integration constants in equation 18. In determining these constants, Plote departed from the fact that the entire heat generated flows into the contacting surfaces (20) and that heat fluxes are distributed to the same measure between the surfaces (21):

$$-\frac{\partial \theta_1}{\partial y_1} - \frac{\partial \theta_2}{\partial y_2} = \dot{Q}(\bar{x}, z) \quad (20)$$

$$\frac{\partial \theta_1}{\partial y_1} = \frac{\partial \theta_2}{\partial y_2} \quad (21)$$

Now the temperature rise of the contacting specimens can already be determined. By adding the melt temperature thereto, the absolute temperature of the surfaces can be calculated.

3.4.2 Determining Oil Temperature

As a result of internal friction in the oil film and compression, heat is generated, which flows within the oil through heat transport towards the walls and in the direction of motion. This energy balance is described by the correlation termed as energy equation in the EHD theory:

$$\underbrace{-\lambda_{e1} \cdot \frac{\partial \vartheta_1}{\partial y_1} - \lambda_{e2} \cdot \frac{\partial \vartheta_2}{\partial y_2}}_{\text{conduction of heat}} - \underbrace{\rho_F \cdot c_{p,F} \cdot h_0 \cdot v_\Sigma \cdot \frac{\partial \vartheta}{\partial x}}_{\text{convection of fluid}} + \underbrace{\eta_{\text{eff}} \cdot \frac{v_s^2}{h_0}}_{\text{shear of fluid}} + \underbrace{\rho_F \cdot \frac{\partial v}{\partial \vartheta} \cdot \vartheta \cdot h_0 \cdot v_\Sigma \cdot \frac{dp}{dx}}_{\text{compression of fluid}} = 0 \quad (22)$$

In order to solve equation (22), it is required to know the temperature profile of the oil along the height of the film (y direction). Accurate specification thereof requires lengthy calculations. Eller departed from the fact that the oil temperature profile in the lubrication gap can be described by a parabola [15] (see Figure 10). This requires knowledge of the surface temperatures (ϑ_1, ϑ_2) and the median integral temperature (ϑ_L). This latter is unknown, and therefore equation (22) needs to be solved in an iterative manner. The temperature profile of the oil is described by equation (23).

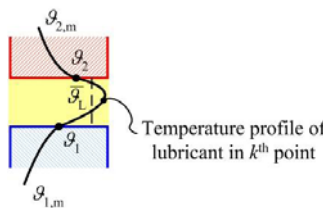


Figure 10
Oil temperature profile in the lubrication gap

$$\vartheta_L(y) = \left(-6 \cdot \bar{\vartheta}_L + 3 \cdot \vartheta_1 + 3 \cdot \vartheta_2 \right) \cdot \left(\frac{y}{h_0} \right)^2 + \left(6 \cdot \bar{\vartheta}_L - 4 \cdot \vartheta_1 - 2 \cdot \vartheta_2 \right) \cdot \frac{y}{h_0} + \vartheta_1 \quad (23)$$

The term caused by compression and included in equation (23) is quite frequently disregarded in the literature due to its insignificance. Oil convection was also

demonstrated to be insignificant compared to the heat fluxes flowing into the walls. In our experience, consideration of the convective member in the case of low film thickness rates (such as the ones at the middle of contact lines) leads to numerical instability. So it is neglected for this reason and with a view to literature data. Accordingly, energy equation (22) is stated in the following form:

$$\underbrace{-\lambda_{c1} \cdot \frac{\partial \vartheta_1}{\partial y_1} - \lambda_{c2} \cdot \frac{\partial \vartheta_2}{\partial y_2}}_{\text{conduction of heat}} + \underbrace{\eta_{E,\text{eff}} \cdot \frac{v_s^2}{h_0}}_{\text{shear of fluid}} = 0 \quad (24)$$

The first two members of equation (24) can be determined on the basis of the oil profile and wall temperatures registered. Oil viscosity depends on both pressure and temperature. The effective viscosity included in equation (24) is the integral mean value of the viscosity values along the height of the lubrication gap. This is why knowledge of the median integral temperature (ϑ_L) is also required for specifying it. As the former is unknown, equation (24) can only be solved iteratively.

The pressure and temperature dependence of viscosity was taken into consideration using the Rodermund equation [16]; this equation assumes the following form:

$$\ln\left(\frac{\eta(\vartheta, p)}{A}\right) = \frac{B}{C+\vartheta} \cdot \left(\frac{p-p_0}{F} + 1\right)^{\left(D+E \cdot \frac{B}{C+\vartheta}\right)} \quad (25)$$

The effective viscosity determined by integrating equation (25) presumes the lubrication oil's Newtonian behaviour. The oil in the lubrication gap is exposed to considerable shear, and therefore it demonstrates non-Newtonian behaviour; this can be taken into consideration by Eyring's material law [14]:

$$\eta_{E,\text{eff}} = \eta_{N,e} \cdot \frac{\frac{\tau}{\tau_{Ey}}}{\sinh\left(\frac{\tau}{\tau_{Ey}}\right)} \quad (26)$$

where τ is oil film shearing, and τ_{Ey} is the Eyring shear stress. This is the stress where the so far Newtonian behaviour of the fluid changes to non-Newtonian.

The equations describing surface temperature rise and median fluid temperature are connected equations to be solved together.

Two examples for the temperatures determined by this method are to be presented, one for the rotational motion of the same direction, the other for the rotational motion of the opposite direction of the rolls.

Figure 11 shows wall and median temperatures as well as the course of effective viscosity in case of rotational motion of the same direction of the rolls within the contact area.

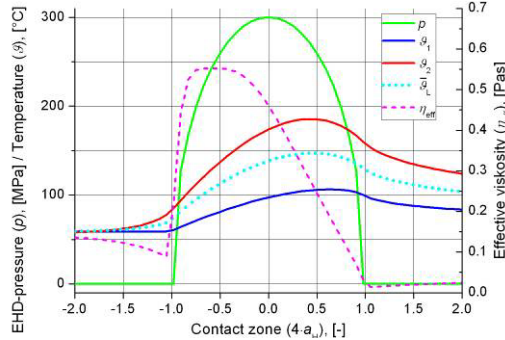


Figure 11

Temperature and viscosity changes in the contact zone in case of rotational motion of the same direction

Figure 12 shows wall and median temperatures as well as the course of effective viscosity in the case of rotational motion of the opposite direction.

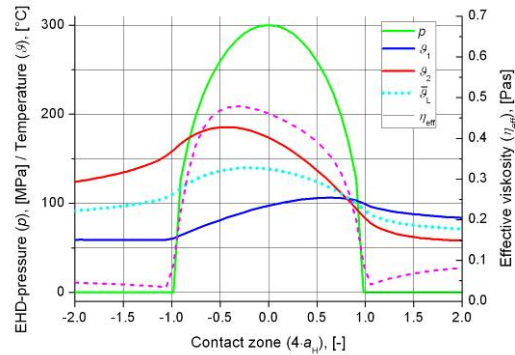


Figure 12

Temperature and viscosity changes in the contact zone in case of rotational motion of the opposite direction

Both the worm shaft and the wheel get more heated up in the case of rotational motion of the opposite direction. Accordingly, the median oil temperature will be higher and the effective oil viscosity will be lower.

3.5 Determining Hydrodynamic Lubrication

Hydrodynamic lubrication arises from film shearing. Shearing is two-directional in the case of worm gear drives, consisting of a component in the direction of motion (x direction) and a component in the direction of the tangent of the contact line (z direction). Taking this and the non-Newtonian behaviour of the oil, shearing stress at a given point of the Hertzian penetration can be specified as follows:

$$\tau_{\text{EHD}} = \sqrt{\left(\tau_{\text{Ey}} \cdot \text{arsinh} \left(\frac{\eta_{\text{Ne}} \cdot v_{\text{tx}}}{\tau_{\text{Ey}} \cdot h} \right) \right)^2 + \left(\tau_{\text{Ez}} \cdot \text{arsinh} \left(\frac{\eta_{\text{Ne}} \cdot v_{\text{tz}}}{\tau_{\text{Ez}} \cdot h} \right) \right)^2} \quad (27)$$

By integrating the (27) equation along the penetration surface, the $F_{\text{F,EHD}}$ frictional force arising from hydrodynamic lubrication is yielded:

$$F_{\text{F,EHD}} = \int_A \tau_{\text{EHD}} \cdot dA \quad (28)$$

Thereby the force arising from hydrodynamic lubrication is known for substituting rolls $F_{\text{F,EHD}}$; the friction coefficient characterizing hydrodynamic lubrication (μ_{EHD}) can already be determined therefrom.

3.6 Determining the Friction Coefficient in Mixed Lubrication

In mixed lubrication, the friction coefficient consists of a component arising from boundary lubrication and one arising from hydrodynamic lubrication. These components are weighted by the function ψ depending on the dimensionless film thickness λ presented above. Hydrodynamic calculations are presented in the previous chapter. Measurement figures are specified by Bouché [4] for boundary lubrication between the tooth flanks of the worm gear drive. According to [4], it ranges between $\mu_{\text{dry}}=0.1 \div 0.14$. For the present investigations, its value was specified at $\mu_{\text{dry}}=0.13$.

As presented above, the coefficient pertaining to the state of mixed lubrication can be determined as follows:

$$\mu_{\text{mixed}} = \psi \cdot \mu_{\text{dry}} + (1 - \psi) \cdot \mu_{\text{EHD}} \quad (29)$$

Figure 13 shows changes – along contact lines – of the friction coefficient determined by the method described above in the case of $n_1=1500$ 1/min input rpm, $T_2=570$ Nm output torque and FVA 4 mineral oil lubrication, at $\vartheta_S=60$ °C oil bath temperature.

As can be observed, in accordance with the partial results presented so far, the friction coefficient assumes its maximum value at the middle of the tooth dominated by boundary lubrication. There are considerable changes in the friction coefficient even along a single contact line.

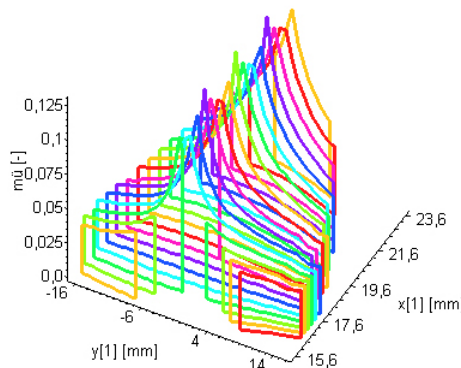


Figure 13
Friction coefficient changes along contact lines (transverse section)

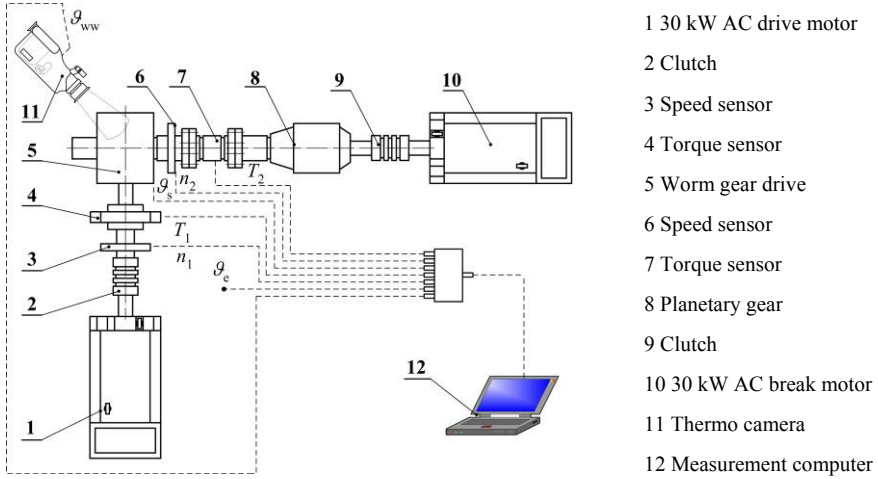
4 Experimental Investigations

The locally changing tooth friction coefficient of worm gear drives cannot be determined directly by gear drive measurements.

The median tooth friction coefficient can be determined indirectly from gear drive efficiency measurements. For this purpose, a test bench was set up at the gear technology laboratory of TU Kaiserslautern Institute of Machine Elements, Gears and Transmissions for testing the efficiency of worm gear drives [17]. The test bench is shown in Figure 14.

In the course of testing, the drive gear set was tested under various torque and rpm loads. Mineral oil with additives of ISO VG 150 viscosity classification was applied as a lubricant, as recommended by the manufacturer. The oil bath precisely covered the worm shaft, and its temperature was set at $\vartheta_S=60\text{ }^\circ\text{C}$.

Worm gear drive losses can be traced back to four basic reasons: losses by tooth friction, oil churning, bearings and shaft seals [18]. Each source of loss can be divided into load dependent (P_{LP}) and no load dependent (P_{L0}) components. The energy balance of the drive gear can be stated on the basis of the input (P_1) and output power (P_2) of the drive gear and sources of loss. The literature provides a number of solutions for defining loss components. Nass set up equations based on measurements to determine load dependent and no load dependent total loss components [19].



These equations were taken as a basis for evaluating our measurements, adjusted to our specific criteria. For the sake of verification, the values thus yielded were compared to the data resulting from the calculations of [18]. Based on the energy balance of the gear drive, tooth efficiency (η_z) can be specified as follows:

$$\eta_z = \frac{|P_2| + |P_{L02}| + |P_{LP2}|}{|P_1| - |P_{L01}| - |P_{LP1}|} \quad (30)$$

The tooth friction coefficient (μ_{zm}) can be calculated from tooth efficiency by taking tooth geometry into consideration as follows:

$$\mu_z = \tan \left(\arctan \left(\frac{\tan(\gamma_m)}{\eta_z} \right) - \gamma_m \right) \cdot \cos(\alpha_n) \quad (31)$$

Thus, efficiency measurements conducted at $n_1=500, 750, 1000, 1500, 2000, 2500$ 1/min input rpm and $T_2=270, 570, 1000$ Nm braking torque yielded the average tooth friction coefficient associated with these load points. By averaging the locally changing tooth friction coefficient determined by simulation to a complete revolution of the worm shaft (summarizing the values of Figure 13 in a single coefficient of friction) an average tooth friction value can be obtained which can be compared to the values measured. The simulation took into account the material properties of FVA 4 mineral oil without additives, as the corresponding data of the mineral oil with additives of ISO VG 150 viscosity classification were not available. Here, it must be taken into consideration that the viscosity of FVA 4 oil is significantly higher than that of the oil used for testing.

Figure 15 shows the values of the average tooth friction coefficient determined for $T_2=270$ Nm load and 5 rpm figures by experimenting and simulation, respectively. The shape of the curves is similar, but it can also be observed that the values measured are overestimated by simulation. The average discrepancy is 0.01.

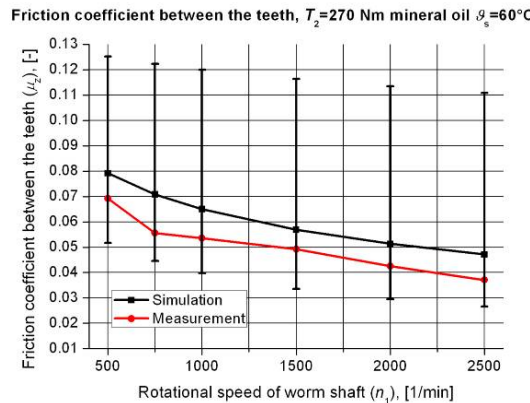


Figure 15
Course of the measured and simulated tooth friction coefficient at 270 Nm output torque

Figure 16 shows the values measured and calculated at $T_2=570$ Nm load. The shape of the curves is similar again, but it is also conspicuous that the discrepancy is getting larger at an increasing rpm.

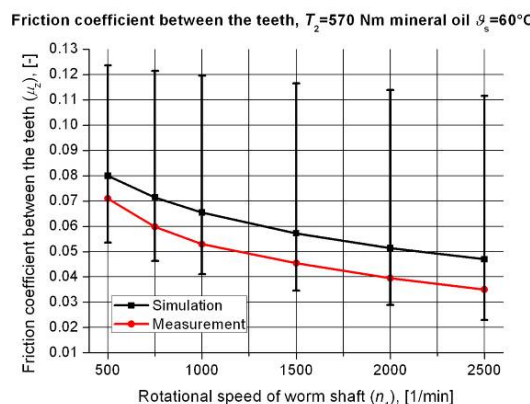


Figure 16
Course of the measured and simulated tooth friction coefficient at 570 Nm output torque

Figure 17 shows the course of the simulated friction coefficients and of the measurement results available at $T_2=1000$ Nm load. Here, the simulation approximates the measured values with the smallest error, although the initial discrepancy corresponds to that of the earlier two loads.

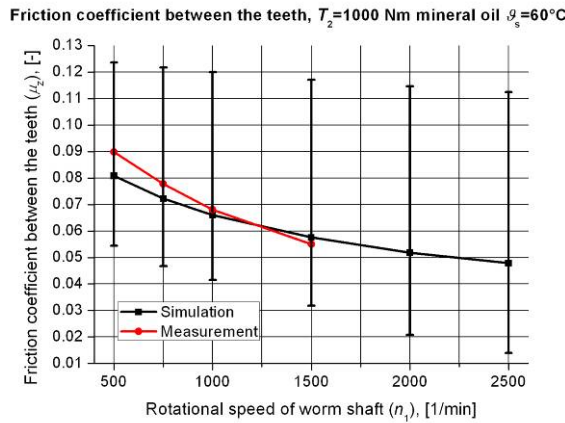


Figure 17

Course of the measured and simulated tooth friction coefficient at 1000 Nm output torque

The measured values were consecutively overestimated by the simulation. This can be attributed to the fact that an oil of higher viscosity was taken into account in the simulation than the oil used for testing. Results can also be affected by the fact that the curve to determine the rate of boundary lubrication models the distribution of asperity heights by Gaussian distribution. The roughness characteristics used for generating substituting surfaces come from 2D roughness measurements. 3D roughness measurements of tooth flanks would yield not only more accurate roughness indices, but would also provide additional information for the statistical description of the height distribution of asperities.

Conclusions

This paper presented a complex calculation procedure to determine the tooth friction coefficient locally changing along the length of the contact lines of worm gear drives. It was also explained how to generate dimensionless Stribeck curves from locally changing tooth friction coefficients determined by such complex calculation; these curves enable the simple still accurate determination of the changing tooth friction coefficient during multibody simulation calculations. The tooth friction coefficients determined by simulation were compared to measured values, and demonstrated satisfactory correspondence.

The authors expect a more accurate agreement by the further development of the calculation algorithm as follows:

- Consideration of the load condition of substituting rolls by load curves based on finite element calculations.
- Application of heat flux distribution changing point by point, describing real conditions more appropriately, in determining surface temperatures.

- Generation of curves to divide boundary and hydrodynamic lubrication using curves based on 3D rough measurements. Assumption of non-Gaussian distribution function if necessary.

Acknowledgements

The authors hereby express their thanks to Dipl.-Ing. Csaba Fábián for his assistance in preparing and conducting measurements. Grateful acknowledgements are also due to Dipl.-Ing. Viktor Aul for useful tribological consultations.

This work was supported by research project OTKA K62875.

References

- [1] Niemann, G.: Schneckengetriebe mit flüssiger Reibung. Berlin: VDI-Verlag 1942
- [2] Wilkesmann, H.: Berechnung von Schneckengetrieben mit unterschiedlichen Zahnprofilformen. Thesis. München: FZG 1974
- [3] Predki W.: Hertzsche Drücke, Schmierspalthöhen und Wirkungsgrade von Schneckengetrieben. Thesis. Bochum: LMG 1982
- [4] Bouché B.: Reibungszahlen von Schneckengetriebeverzahnungen im Mischreibungsgesetz. Thesis. Bochum: LMG 1991
- [5] Johnson K. L.: Regimes of Elastohydrodynamic Lubrication. Journal Mechanical Engineering Science 12 (1970) 1, pp. 9-16
- [6] Litvin F. L., Fuentes A.: Gear Geometry and Applied Theory. Cambridge: University Press 2004
- [7] Weisel, C.: Schneckengetriebe mit lokal begrenztem Tragbild. Thesis. München: FZG 2009
- [8] Venner C. H.: Multilevel Solution of the EHL Line and Point Contact Problems. Thesis. Twente: Emschede 1991
- [9] Murch L. E., Wilson W. R. D.: A Thermal Elastohydrodynamic Inlet Zone Analysis. Transaction of the ASME (1975) 4, pp. 212-216
- [10] Wiśniewski M. Elastohydrodynamische Schmierung. Renningen-Malmsheim: Expert Verlag 2000
- [11] Greenwood, J. A.; Williamson, J. B. P.: Contact of Nominally Flat Surfaces. Proceedings of the Royal Society of London. Series A, Mathematical and Physical Sciences. Vol. 295, pp. 300-319, 1966
- [12] Whitehouse, D. J.; Archard, J. F.: The Properties of Random Surfaces of Significance in their Contact. Proceedings of the Royal Society of London. Series A, Mathematical and Physical Sciences. Vol. 316, pp. 97-121, 1970

- [13] Gnilke, W.: Theorie der Mischreibung. Freiberger Forschungshefte: Theorie der Mischreibung und ihre Anwendung auf Gleitlager. Leipzig: VEB Deutscher Verlag für Grundstoffindustrie 1982
- [14] Plote, H.: Zur Berechnung Thermo-Elasto-Hydrodynamischer Kontakte. Thesis. Clausthal: IRM 1997
- [15] Eller, G.: Ein Beitrag zur Berechnung des stationären, nichtisotermen elastohydrodynamischen Schmierfilms. Thesis. Karlsruhe: IML 1987
- [16] Rodermund H.: Extrapolierende Berechnung des Viskositätsverlaufes unter hohen Drücken. Tribologie und Schmierungstechnik 27 (1980) 1, pp. 3-5
- [17] Magyar, B.; Horák, P.; Sauer, B.; Fábián, Cs.: Experimentelle Untersuchung der Zahnreibungszahl von Schneckengetrieben mit der Flankenform K. GÉP LXI (2010) 9-10, pp. 51-54
- [18] E DIN 3996:2005-08 Tragfähigkeitsberechnung von Zylinder-Schneckengetrieben mit sich rechtwinklig kreuzenden Achsen. Beuth-Verlag: Berlin 2005
- [19] Nass U.: Tragfähigkeitssteigerung von Schneckengetrieben durch Optimierung der Schneckenradbronze. Thesis. Bochum: LMGK 1995